DOI: 10.13009/EUCASS2023-689
Aerospace Europe Conference 2023 – 10TH EUCASS – 9TH CEAS

Analysis of Process Parameters Effects on Final Properties of Additively Manufactured Components for Space Applications

Davide Zuin[⋆†], *Simone La Luna*[⋆], *Filippo Maggi*[⋆], *Nicola Sicignano*[⋆⋆], *Domenico Borrelli*[⋆⋆]
[⋆]*Politecnico di Milano, Via La Masa 34, 20156 Milano (MI), Italy*
[⋆⋆]*Sòphia High Tech, Via Malatesta, 30A, 80049 Somma Vesuviana (NA), Italy*
davide.zuin@polimi.it · simone.laluna@polimi.it · filippo.maggi@polimi.it
nicola.sicignano@sophiahightech.com · domenico.borrelli@sophiahightech.com
[†]Corresponding author

Abstract

This paper presents an analysis of the criticalities associated to AM SLM machine process parameters for metals within space propulsive applications through a dedicated design of experiment. Inconel 718 is considered: the effects of manufacturing process parameters on the final metallurgical properties of a part are discussed through dedicated samples printing. A skin-core scan strategy is applied to evaluate specimens' internal part (body) and external (contour) parameters separately. The target is the definition of a proper processing window for the two areas in terms of laser power, scan speed, hatch space where optimized parameters lead to minimal defects on samples. In particular, the influence of the process window on the final samples' dimension, density, porosity and hardness is evaluated, leading to the selection of a subset of process data feasible for space propulsive components manufacturing.

1. Introduction

Within the last decade, applications of metal Additive Manufacturing (AM) Selective Laser Melting (SLM) in the space propulsive panorama have become widespread. The design possibilities enabled by this technology, such as production of complex, robust and high-performance combustion chambers and nozzles, are being exploited within research institutes and industries as well.[1–3] Despite the technology is well established in the market, the characterization of the process and its impacts on the final properties of parts are still topics of discussion.[4] Challenges at processing and supply chain levels and their impacts on the final components become important when critical propulsive components are considered. In SLM for propulsive applications, high-strength nickel-based superalloys are generally implemented.[1,5,6] Among these materials, Inconel 718 (IN718) stands for its capabilities of withstanding extreme temperatures and corrosive environments while maintaining good mechanical strength. IN718 is a precipitation strengthened alloy which is characterized by a general FCC γ austenite matrix including γ' and γ'' strengthening phases as well as other entrainments.[7,8] The design capabilities of additively manufacturing this material are exploited in space propulsive components to obtain convoluted channels geometries for regenerative cooling of thrust chambers and nozzles as well as small wall thickness surfaces to improve heat exchange between cooling channels and combustion areas.[1,2] Full parts with correct final design dimensions shall be considered with these critical components.
Considering the SLM process involving metallic materials, control strategies of specimens final properties affect the most prominent parameters, namely machine laser power and laser scanning speed. These parameters are combined to retrieve the Linear Energy Density (LED) associated to the process.[4] This latter parameter may be used as an initial guess to ensure good process formability: low power or high scan speed would decrease the amount of energy supplied to the material leading to increased defects such as lack of fusion. On the other hand, discontinuous tracks due to poor surface tension interactions tend to create bead-shape spots that might block the printing process due to an increment of layer thickness, and the insurgence of balling phenomena.[9,10] Excessive balling is associated to increased surface roughness and excessive porosity of the final components. An increase in laser power has demonstrated to reduce balling while leading to the insurgence of keyhole defects, due to vaporization of light elements in the molten material.[10,11] Specific tuning of these parameters is mandatory to avoid the formation of internal or superficial defects on sample specimens. However, other characteristics of SLM processing shall be considered during the printing process. Parameters such as hatch spacing and layer thickness might alter the results obtained from LED analysis. These are

DOI: 10.13009/EUCASS2023-689

added and combined to the previous considerations in order to retrieve the Volumetric Energy Density (VED) formula:

$$VED = \frac{P}{v \cdot h \cdot t} \tag{1}$$

where P stands for laser power, v is the scanning speed, h is the hatch spacing and t the layer thickness of the powder bed.[12, 13]

Within the present work, characterization of IN718 samples printed through an AM SLM machine involved in the processing of components for space propulsive applications is detailed. The aim of the study is the influence evaluation of machine process parameters in order to find optimized values that maximize compactness of final specimens. Further aim is the definition of process parameters for contour as well, determining correlations between process parameters and final dimensions of samples. Parameters are selected from a range of laser power, scan speed, and hatch spacing values corresponding to different VED results. The study allows a more detailed comprehension of the AM process effects on final as-built components through a procedure which identifies the most suited parameters for AM of space propulsive components.

2. Experimental Design

The work has considered a specific Design of Experiment (DoE): a series of jobs were printed through a Concept Laser M2 Series 3 machine. Virgin IN718 powder was retrieved for all the jobs: its chemical properties are resumed in Table 1. The particle size distribution values of the selected IN718 powders was primarily distributed in the range of 16 - 55 μm. Investigation results include micrography and density evaluations, porosity on metallographic sections, hardness testing and optical inspections for dimensional measurements. A skin-core scan strategy (also known as contouring strategy) has been implemeneted. It consists in the division of components into two separate regions, where process parameters are optimized separately. This strategy allows for the separation of criticality assessment in three parts: the analysis of body parameters, the analysis of contour parameters and the interactions among them (overlap region). A schematic representation of the areas is reported in Figure 1.

2.1 Cubic Samples

In order to study the body parameters, a series of two prints including cubic samples, each one of $15mmx15mmx15mm$ side, were performed. Three variables have been investigated, namely laser power, scan speed and hatch spacing.

Table 1: IN718 powder chemical composition analysis: data are reported in weight percent, w.t.%.

Parameter	Al	Ti	O	N	Nb+Ta	Ni	Mo	Mn	Cu	Co	Cr	C
Min	0.20	0.65	0.00	0.00	4.75	50.00	2.80	0.00	0.00	0.00	17.00	0.00
Max	0.80	1.15	0.03	0.03	5.50	55.00	3.30	0.35	0.30	1.00	21.00	0.08
Result	0.54	0.98	0.02	0.01	4.99	53.46	3.08	< 0.08	< 0.10	< 0.20	20.00	0.04

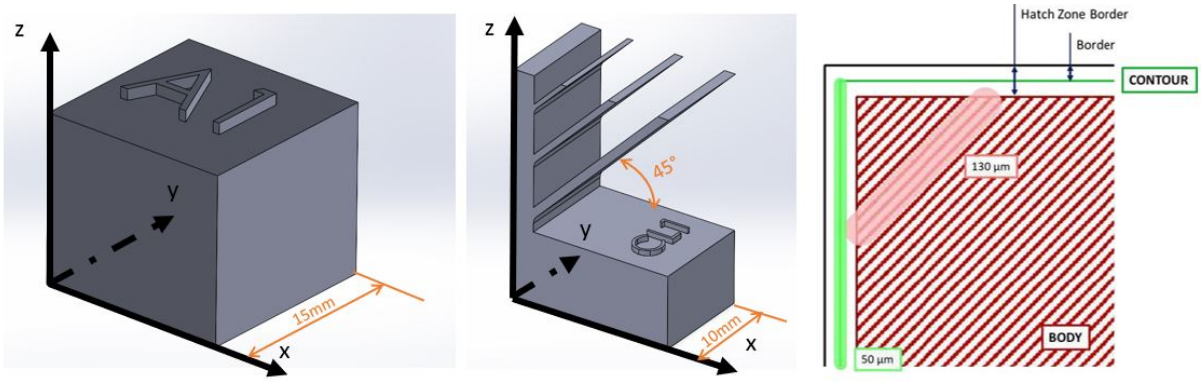

Figure 1: Description of the printed specimens: cubic samples for body evaluation on the left; inclined walls samples for contour evaluation at center; description of the skin-core scan strategy on the right. Core is identified in red, with spotsize highlighted with the red marker; skin is identified in green, with spotsize highlighted with the green marker. HZB and border are identified.

DOI: 10.13009/EUCASS2023-689

Table 2: Cubic sample body parameters. Fixed layer thickness of 25μm and spotsize of 130μm are considered.

Sample ID [−]	**Spot Size** [μm]	**Layer Thickness** [μm]	**Power** [W]	**Scanning Speed** [mm/s]	**Hatch Spacing** [mm]	**VED** [J/mm^3]
1			250	800	0.1	125.00
2			200	1200	0.09	74.07
3			200	800	0.09	111.11
4			200	1000	0.09	88.89
5			200	1000	0.1	80.00
6			150	1000	0.09	66.67
7			200	1000	0.08	100.00
8	130	25	150	800	0.1	75.00
9			150	800	0.08	93.75
10			250	1200	0.1	83.33
11			250	1200	0.08	104.17
12			250	1000	0.09	111.11
13			250	800	0.08	156.25
14			150	1200	0.08	62.50
15			150	1200	0.1	50.00

Layer thickness and machine laser spotsize were considered fixed at 25 μm and 130 μm respectively. Selection of the proper parameters to be implemenetd in the design of experiment for the cubic samples has started considering previous studies on IN718. Yi et al.[14] have demonstrated highest relative density for a LED value corresponding to $0.2 J/mm$ while the best stacking of multiple molten pools was obtained at LED of $0.3 J/mm$. A similar result was achieved by Kumar et al.[15] where the optimal LED value was settled in the range of $0.27 - 0.35 J/mm$, as well as from Liu et al.[16] As a result, a range of laser power and scanning speed values was selected. On the hatch spacing, literature analyses[17] show that values of 30% overlap between two adjacent molten tracks shall be achieved:

$$\delta = \frac{d - h}{d} \tag{2}$$

where δ is the overlap ratio, d the laser spot diameter and h the hatch distance defined as:[18,19]

$$h = 0.7d \tag{3}$$

The selected laser power values are tuned between 150W and 250W; laser scan speed between 800mm/s and 1200mm/s; the hatch distance (following Equation 3) between 0.08mm and 0.1mm. In order to discretize the selected ranges, a number of 15 samples was selected following a Face-centered Central Composite Design (FCCD). The selected values of laser power, scan speed and hatch spacing for the DoE are resumed in Table 2. Within the first of the two prints, the original base plate has been divided into four areas in order to study the effect of building position inside the printing volume as well: specimen disposition in this build job is reported in Figure 2. As it is depicted in the image, the set of 15 cubic samples is repeated four times to cover the overall build plate: a total amount of 60 cubic samples is retrieved. The second print of the DoE includes a subset of cubic specimens, the one which show consistent results in terms of dimensional, density and porosity repeatibility between the four areas. Within the second job, the build plate area repetition has been discarded. For all the specimens, a skin/core scan strategy has been selected for the study: in particular, the body (core) of the specimens has been printed with a meander path of 45 degrees with interlayer rotation. Contour (skin) path has been compensated using the machine software. For all the cubic samples, contour parameters have been fixed with laser power of 180 W, laser speed of 1000 mm/s and spotsize of 50 μm. All samples have been rotated around the Z-axis by 10 degrees in order to preserve the recoater blade integrity with less surface interaction.

2.2 Contour and overlap region

Contour parameters are verified through inclined walls samples with 45 degrees inclination and thicknesses of 0.8mm, 0.6mm and 0.4mm respectively, as reported on Figure 1. Samples are inserted in a third and separate job with respect to the cubes, in order to properly space them within the job plate and avoid deterioration of the surface finish of the specimens due to recoater erosion or coalesced powder. The contour parameters were selected starting from literature review analysis.[20] A spotsize of 50 μm and laser power of 180 W were fixed while varying the laser scanning speeds between 600 mm/s and 2000 mm/s. Variation of the Hatch Zone Border (HZB) and border dimensions have been

DOI: 10.13009/EUCASS2023-689

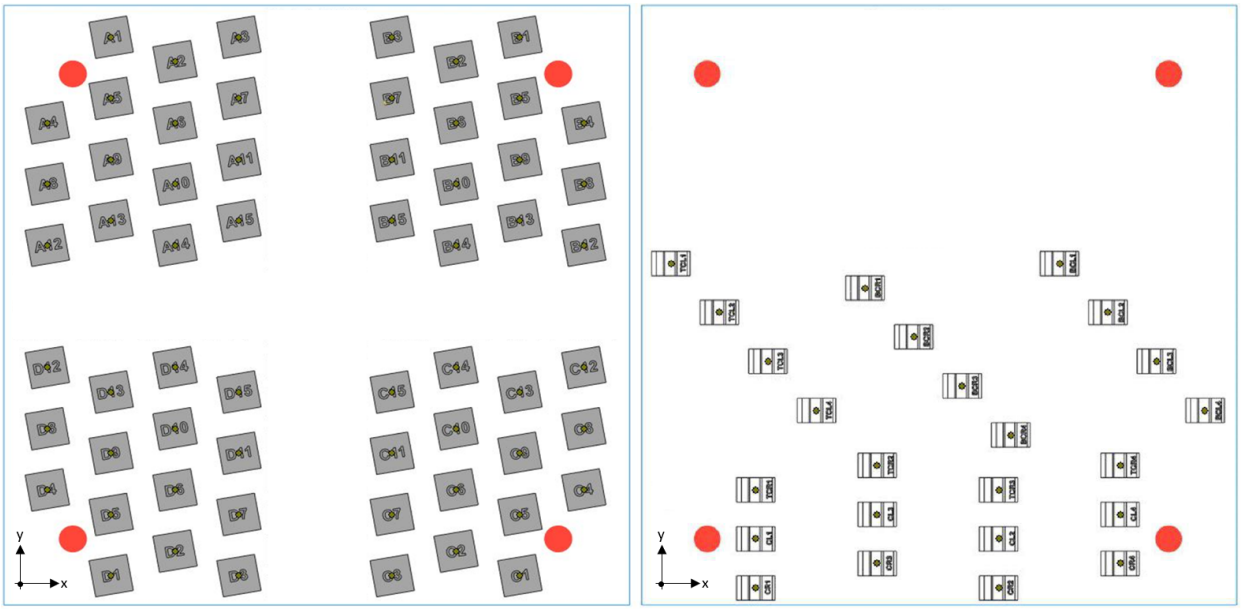

Figure 2: Job plates details. On the left, print job of cubic samples: four areas are identified and coded with letters A, B, C and D which stand for top left, top right, bottom right and bottom left positions on the plate respectively. Each cube in any area is numbered from 1 to 15, following the parameters detailed in Table 2. On the right, print job disposition of inclined surfaces samples: each specimen is associated to a family letter and a group number as detailed in Table 3.

Table 3: Contour parameters. Each HZB - border group (number 1 to 4) is applied to a selected scan speed family (letter CL to BCL) to obtain 24 inclined walls specimens. Definition of HZB and border are highlighted in Figure 1.

Scan Speed						
Family	CL	CR	TCL	BCR	TCR	BCL
Scan Speed, $[mm/s]$	600	800	1000	1200	1600	2000
Hatch Zone Border						
Group			1	2	3	4
Hatch Zone Border, $[\mu m]$			170	140	110	80
Border, $[\mu m]$			85	70	55	40

considered, as defined in Figure 1. Six (6) scan speed families were associated to four (4) HZB and border parameters to obtain 24 samples. Parameters of this DoE are a combination of the data noted in Table 3. For each specimen it was also considered a beam compensation value equal to half the contour spot size:

$$Border = \frac{HZB}{2} \tag{4}$$

For the contour specimens, body parameters with a fixed spotsize of 130 μm, laser power of 180 W, laser speed of 800 mm/s have been considered.

3. Result and Discussion

3.1 Body Results

Cubic specimens have been evaluated in their nominal dimension and final quality of the printed samples. The effects due to distribution on the plate were investigated as well. The target of this analysis is the determination of optimized core parameters in terms of laser power P, scan speed v and hatch spacing h as defined in Equation 1 and depicted in Figure 1.

DOI: 10.13009/EUCASS2023-689

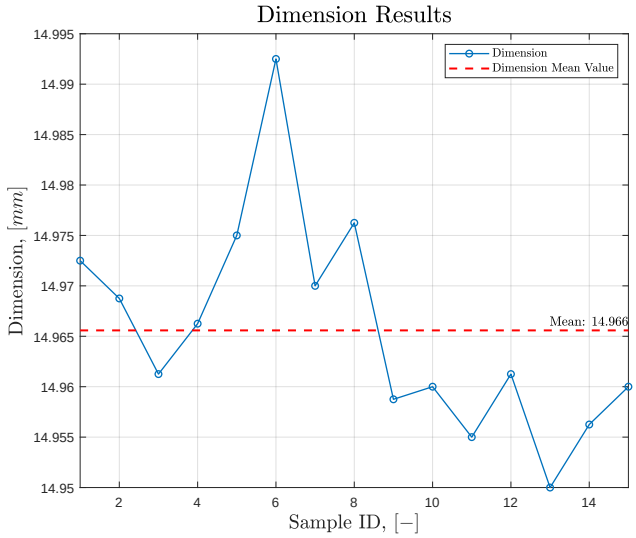

Figure 3: Cubic samples dimension measurements: mean values plot. The dotted red line reports the mean value among all specimens, which is lower than the desired nominal dimension.

3.1.1 Distribution Effects on the Plate

Test result analysis starts with the determination of dimensional, density and porosity distribution on the build plate. Starting from the cubes' **dimensional test**, measurements were taken on each cubic sample along x and y direction of the building plate using a micrometer. The nominal dimension of the cube, highlighted in Figure 1, was then compared with the results. The final mean value of XY dimensions are reported in Figure 3. The mean values have been calculated for each parameter set making an average of six (6) of the eight (8) taken measurements (the maximum and minimum outliers have been discarded). The mean value was computed and reported in Figure 3. Considering that there should not be any dependency from the body parameters and from the building plate position, the variability shown is related only to the superficial roughness and the defined contour parameter set. More in detail, the selected contour offset parameters (equal for every cubic sample) are probably too high: there is a mean nominal dimension reduction of about 0.04 mm from the nominal desired dimension.

Density tests were performed on the samples using a Gibertini Europe 500 scale. The process included the measurement of samples in air then in demineralized water, considering the difference among the two measures. For each sample, five (5) readings were retained and results finally averaged. Density values for each cubic sample are resumed in Table 4. As it is shown, the percentage values are reported with respect to the full density of Inconel 718 of $8.220 g/cm^3$. The result shows clear improved percentage values when considering samples 1, 3, 10, 11, 12, 13: these samples are characterized by the highest selected VED values. A clear relation between higher densification and higher beam energy is confirmed, as stated in other studies.[4] In order to further highlight the dependencies between density results and process parameters, densification data can be compared with the single independent variables: laser power, scan speed and hatch spacing. Density values tend to be spread when compared to samples printed with the same scanning speed and hatch spacing; on the contrary, similar values are recovered when comparing density values with laser power. Furthermore, laser power seems to significantly affect the density of the samples: average density values of 97.50% and 99.55% are retrieved when considering 150W and 250W laser power respectively, improving the results of more than 2%.

Finally, the dependency on the plate disposition is analysed: specimen results are compared depending on their position on a different layout area. Concerning densification, outcomes are graphically resumed in Figure 4. From the left picture, it is evident that results on density determination by hydrostatic weighing are not significantly affected by the plate disposition. This highlights that density values are mainly related to the selected process parameters and are not impacted on their disposition on the plate. Phenomena related to the machine (e.g. laser focusing and simmetry on the plate, recoater deposition patter), if present, do not significantly affect the final results.

After the density tests, more in-depth analyses of the porosity distribution on metallographic sections have been performed according to the technical document VDI 3405-2. The analysis aimed at the estimation of the voids on metallographic sections considering five (5) fields for each sample with approximate dimensions of $1,5mmx2,0mm$ evenly

DOI: 10.13009/EUCASS2023-689

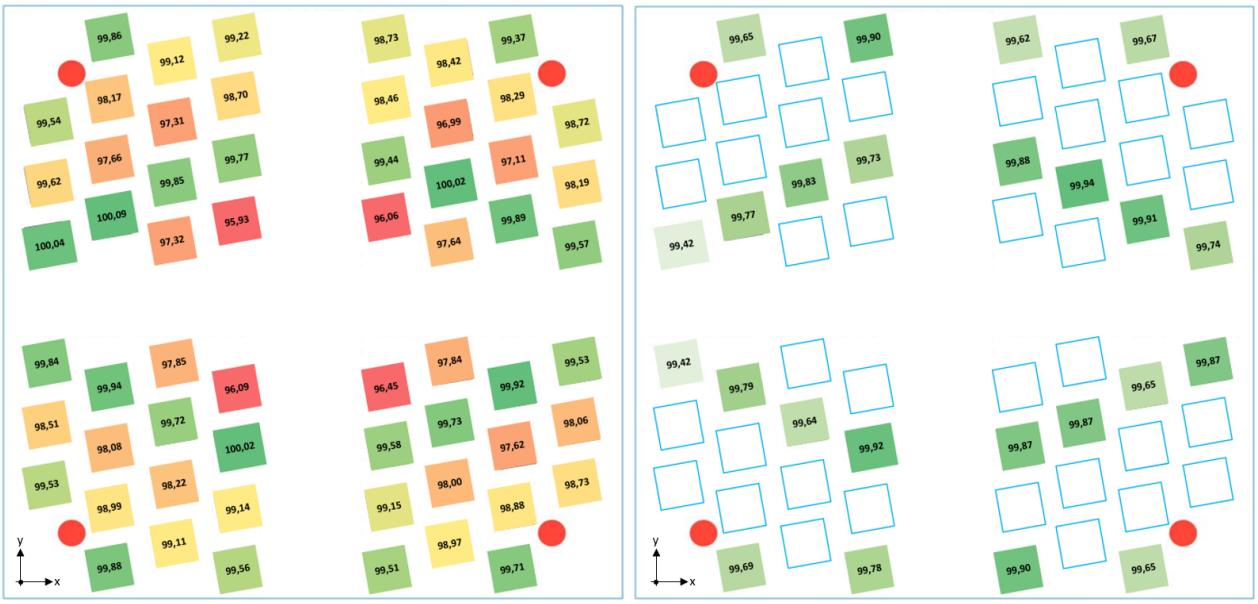

Figure 4: Cubic samples dependance on build plate position: on the left, density measurement percentages on all samples; on the right, porosity measurement percentages on the selected subset of specimens.

Table 4: Cubic samples density measurements in g/cm^3: mean values are reported for cubes in each of the four areas of the plate. Column letters stand for the position zones on the plate, as reported in Figure 2. Sample 1, 3, 10, 11, 12 and 13 show the highest densification values.

	A	**B**	**C**	**D**	**Mean**	**Percentage**
1	8.2093	8.1694	8.1969	8.2112	8.1967	99.71%
2	8.1482	8.0908	8.1365	8.1477	8.1308	98.90%
3	8.1564	8.1167	8.1805	8.1848	8.1596	99.25%
4	8.1830	8.1160	8.1167	8.1822	8.1495	99.13%
5	8.0705	8.0803	8.1292	8.1381	8.1045	98.58%
6	7.9997	7.9738	8.0567	8.0747	8.0262	97.63%
7	8.1142	8.0943	8.1506	8.1503	8.1273	98.86%
8	8.1074	8.0719	8.0612	8.0988	8.0848	98.34%
9	8.0286	7.9835	8.0257	8.0629	8.0252	97.62%
10	8.2083	8.2226	8.1984	8.1976	8.2067	99.83%
11	8.2018	8.1752	8.1861	8.2223	8.1963	99.70%
12	8.2240	8.1855	8.1819	8.2077	8.1998	99.74%
13	8.2283	8.2118	8.2143	8.2158	8.2175	99.96%
14	8.0002	8.0266	8.0436	8.0440	8.0286	97.66%
15	7.8866	7.8974	7.9290	7.8993	7.9030	96.13%

distributed on the sample section. For each specimen, the section parallel to the building plate was considered. Each field was observed using an optical microscope Nikon Eclipse LV150N with 50x magnification. The images were post-processed through imageJ software[21] and the percentages of voids were averaged on the five fields to obtain a single value for each sample. Only specimen 1, 3, 10, 11, 12, 13 were considered in this analysis since, from the previous analysis, they showed higher density results. Data are reported in Figure 4.
From data analysis, it is clear that porosity values on the sections are all above 99%, independently from the sample parameter and the plate disposition. This confirms that specimens with the five selected parameters show consistent data with their density results.

3.1.2 Densification Comparison

As minor impacts were measured by the plate disposition results in terms of density and porosity, a new print of the cubes was performed. The new job was deemed necessary to focus the study on a reduced number of samples, con-

DOI: 10.13009/EUCASS2023-689

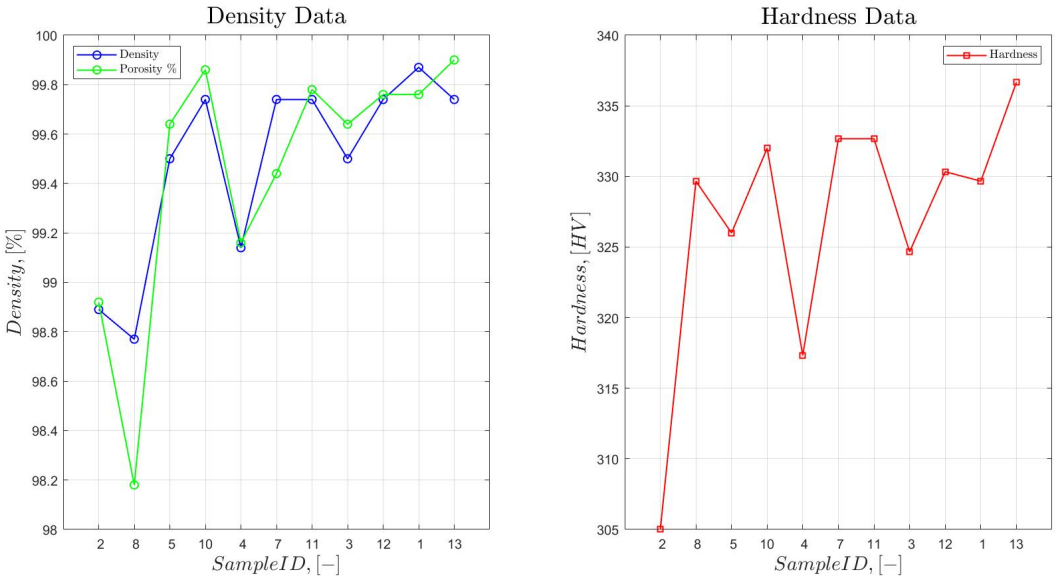

Figure 5: Main results on density, porosity and hardness on the eleven samples from the second build job. On the left, density through hydrostatic weighing (in blue) and porosity percentage (in green); on the right, hardness values (in red).

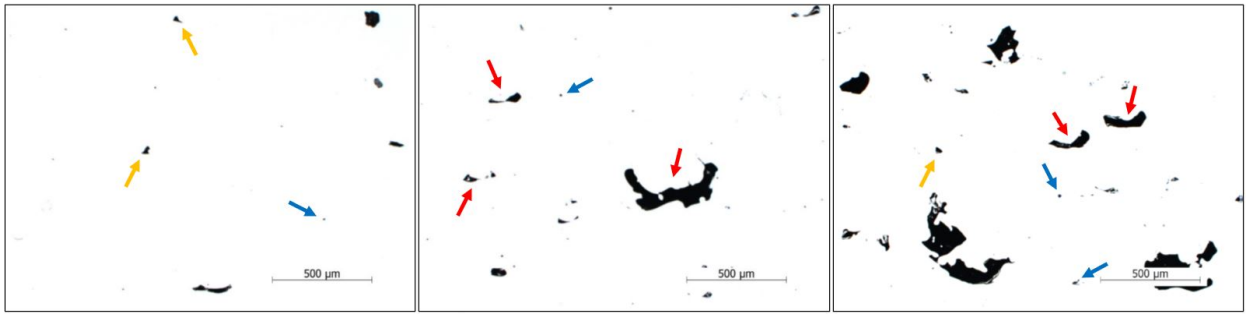

Figure 6: Optical images of metallographic sections after postprocess: laser power is fixed at 200 W and hatch space 0.09 mm for the three fields. From the left to the right: scanning speed is 800 mm/s, 1000 mm/s and 1200 mm/s respectively. Blue arrows mark gas entrapments; orange arrows mark open pores; red arrows mark horizontal lack of fusion.

centrating the analysis effort on the determination of densification results and their relations with machine parameters. Plate division and sample repetition on the build plate was discarded: samples were evenly distributed on the entire build job. Parameters which showed the worst results in terms of density, namely sample 6, 9, 14 and 15, were not considered and only eleven (11) specimens were printed. Test results on density and porosity on metallographic sections were repeated, according to the aforementioned procedures: they are briefly summarized in Figure 5.

In the graph, specimens are numbered according to increasing VED data. Density percentages are consistent with previous results; furthermore, previous dependency between density values and VED is confirmed. In particular, density changes of more than 1.5%, a value which is similar to the previous job. A trend can be highlighted between samples, were specimens 2, 8, 5 and 4 display lower density results compared to the others, sometimes even dropping below 98.5%.

Similar conclusions are highlighted for porosity percentages. Defects which can be recognized from optical images of samples' metallographic sections are of different nature,[22] as shown in Figure 6: gas porosity, open pores and lack of fusion can be noticed. Gas porosities (blue arrows) are formed when shielding gas is enclosed in the material during the solidification process. The same defect may originates when internal gas is trapped within powder particles, then molten by the laser. This defect can be recognized by the spherical shape of the entraiment and are present on all the images independently from the selected scanning speed. Open pores (orange arrows) are identified in images with high energy densities. They are generated during the process as the molten fluid is pushed toward the periphery by

DOI: 10.13009/EUCASS2023-689

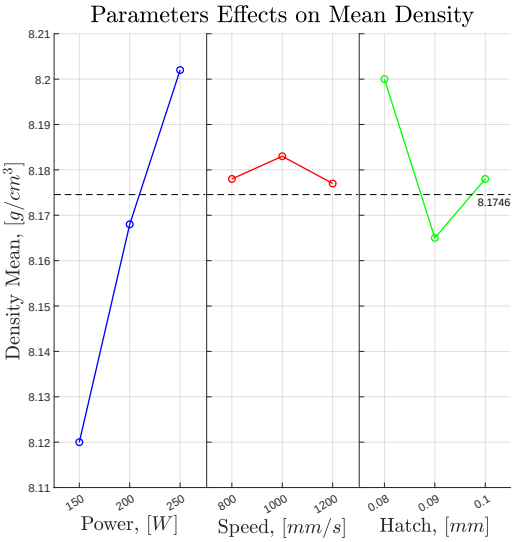

Figure 7: Main effects of individual independent variables on hydrostatic weighing density. The impacts of laser power, scanning speed, and hatch spacing are presented in the left, center, and right graphs, respectively. From the results, it is clear that the effect due to laser power is predominant with respect to the other parameters.

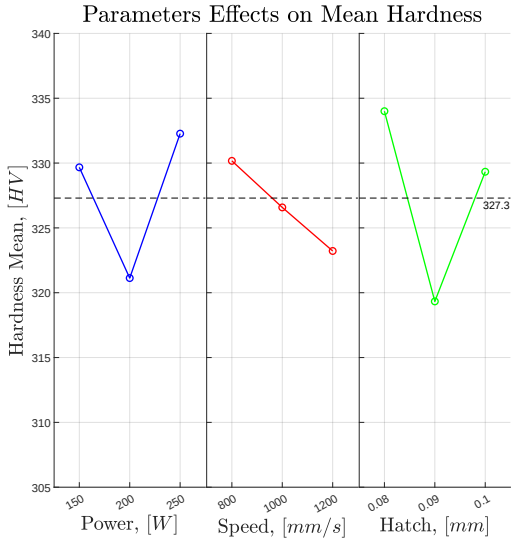

Figure 8: Main effects of individual independent variables on hardness. The impacts of laser power, scanning speed, and hatch spacing are presented in the left, center, and right graphs, respectively. From the results, it is clear that no predominant effect can be recognized between parameters.

the laser: solidification rate does not allow the refilling of the gap, which is then noted as open pore in the sample.[23] Finally, lack of fusion (red arrows) are present, which tend to increase in dimension as energy density decreases. Some of the defects of this type show internal powder partially melted. The origin of these defects can be traced back to poor remelting and adhesion between layers, low powder bed density (due to deposition issues or powder removal by overpressure issues during the process), laser focusing issues due to attenuation of the beam (from vapour or improper focusing), large hatch distance, other.[4,24]

The dependency between low VED values and increased porosity can be further tailored to the single parameters impacting the VED definition. As shown in Figure 7, it is evident that the power value significantly influences the observed results. Its impact on densification is pivotal, shifting density results from 98.65% to 99.75%. Altough scanning

DOI: 10.13009/EUCASS2023-689

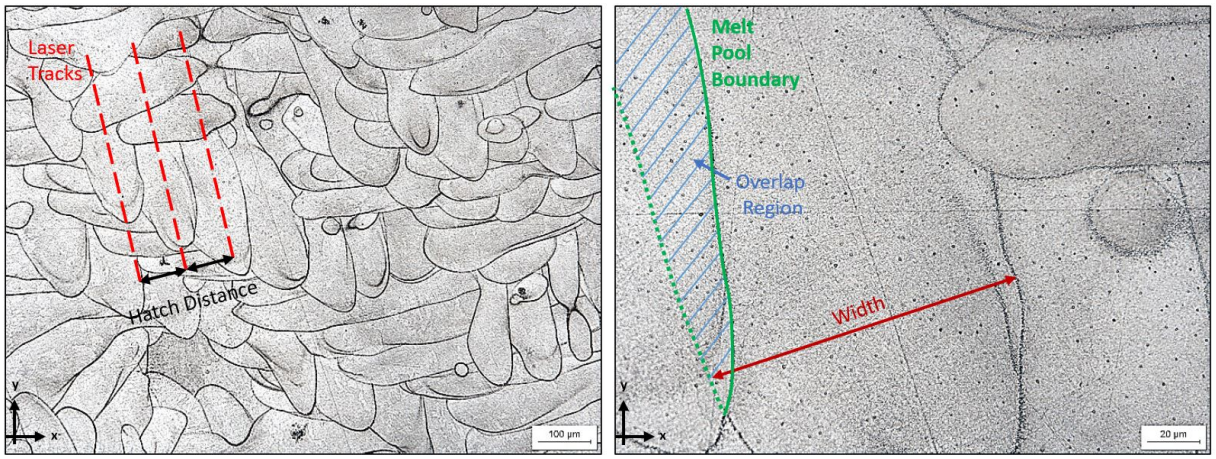

Figure 9: Micrographic images of specimen 11. Images have been retrieved at the center of the cubic sample. On the left, micrographic image of XY plane; the laser tracks are evidencied in red, while the hatch distance in black. On the right, magnification of the left image at the center; width of the melting pools and overlapping regions are identified in red and blue respectively.

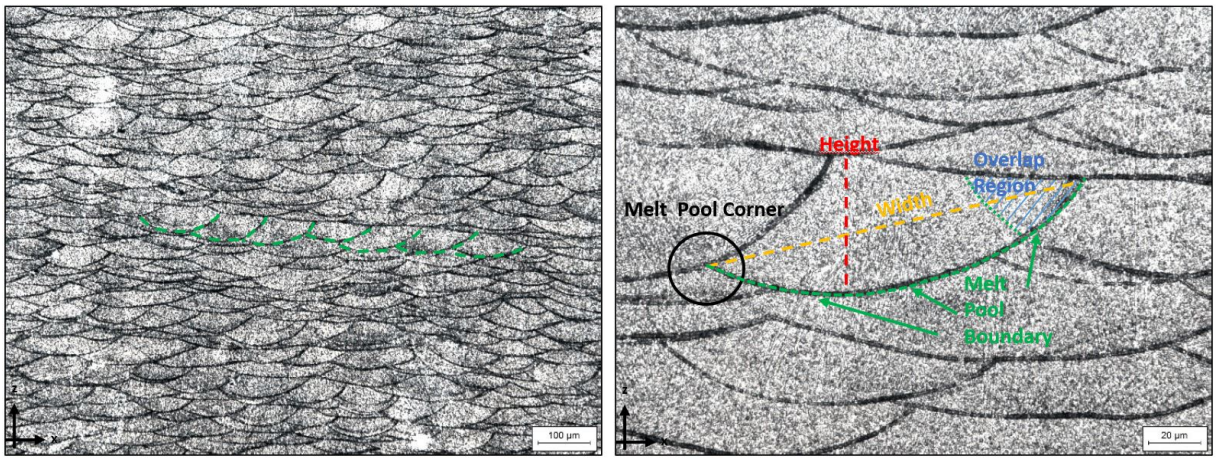

Figure 10: Micrographic images of specimen 11. Images have been retrieved at the center of the cubic sample. On the left, micrographic image of XZ plane; overlapping melting pools boundaries are highlighted in green. On the right, magnification of the left image at the center; height and width of the melting pools are highlighted in red and yellow respectively, overlapping regions in blue and melt pools corner in black.

speed impact can be recognized in Figure 6, it seems to only secondarily affect densification values. Finally, hatch spacing variation reports contradictory results and it has a lower effect on density of cubic samples.

Further data on the body parameters have been retrieved considering metallographic images. **Micrographic examination** of the samples were carried out on the metallographic specimens obtained from the transverse and longitudinal sectioning of each of the 11 cubic specimens, mounted in resin and properly polished. Micrographic analyses included optical images at 100x and 500x magnification with a light microscope Olympus BX51M. Metallographic etching was performed on the samples using waterless Kalling's reagent No. 2 (5g of $CuCl_2$, 100ml of HCl and 100ml of ethyl alcohol). All samples shown a microstructure consisting of a metallic matrix of austenitic phase (γ phase) with dispersed columnar precipitates, typical of Inconel 718 without thermal postprocesses.[7]

From micrographic images of XY plane (see Figure 9), laser tracks can be highlighted: the repeatibility of the hatch distance between tracks can be noted as well. From these images, tracks are properly superimposed on all the specimens, suggesting an optimized window of hatch distance parameters. Usually, melting pool boundaries and overlap regions require attention, as they are reknown to impact reliability and quality of final components. In particular, overlap regions are affected by remelting and heating constrains, which impact the formation of pores and lack of fusion defects. These tend to concentrate at the corner of melting pool boundaries, where overheating may occur.[22,25] Micrographic images in this DoE show limited defects of this type, suggesting minor impacts of hatch distance on sample

DOI: 10.13009/EUCASS2023-689

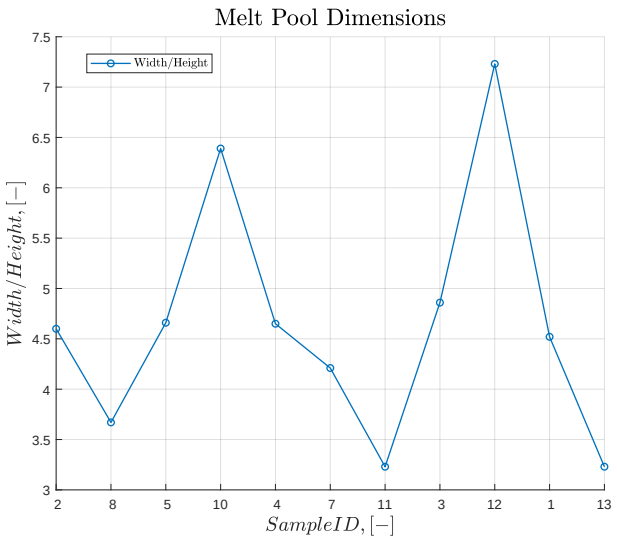

Figure 11: Width over height computation for the specimens melt pools. Sample 10 and 12 show flattened melting pools with respect to the other specimens, leading to higher width over height values.

densification. This further confirms previous results on sample properties distribution.
Within the micrographic images on XZ plane (see Figure 10), laser multi-track are highlighted: each adjacent scanning track result in a melting pool which, after solidification, is larger than laser spotsize. Remelting of previous layers is noted as well, in particular in the overlap regions: this is due to higher penetration of the laser pool with respect to layer thickness.[4] All the samples sectioned in the transverse direction have shown consistent overlapping layers, which can be highlighted by the melting pool boundaries in Figure 10. As from the fields in XY direction, only minor presence of voids or air pockets within the printed part are registered among molten tracks.
A preliminary comparison analysis of the morphology of the molten tracks is reported in Figure 11. For each micrographic image, the width and height of seven (7) molten pools was retrieved, then the averaged values were compared to identify relations between the process parameters and the final build objects. This method is already implemented in literature to compare molten tracks with different parameters.[4,25] It is derived from NASA MSFC-SPEC-3717 technical document, which recommends to use an increased number of tests and single tracks. In this case, the method has been applied to as-built multi-tracks metallurgical samples: depending on the process parameters, melting pools are affected by remelting phenomena as well as heating of the previous layers, an effect which is assumed to only secondarily impact on the melt pools layout within this analysis. From the graph, some of the samples show a flattened and less homogeneous morphology of the melting pools with respect to other specimens: it is the case of samples 10 or 12, that report width-over-height values higher than the other specimens. Such structure morphology may not be suitable for ensuring the desired mechanical properties of the material. However, in order to verify this assumption, further in-depth analyses are required, focusing on single track determination.

As final analysis, **hardness vickers tests** were performed on the 11 samples, at the center of the XZ section. The test involved a hardness testing machine KB Pruftechnik and were performed according to test standard UNI EN ISO 6507-1. A 10kg load was implemented. Each test was repeated three times and the value averaged on the three readings. Final results are resumed in Table 5 and Figure 5. The hardness measurements show minor differences between the printed sample: all the results are consistent with reference values retrieved for additively manufactured as-built IN718 samples.[7,26] It is worth noting that a similar behaviour between density, porosity on metallographic sections and hardness is registered among samples. However, contrarily to the first two parameters, hardness values tend to be significantly susceptible to VED data. When VED increases, hardness values tend to increase as well. This is evident by the results reported in Figure 8, where a comparison between hardness and the single independent variables is performed. Thermal phenomena may be related to this behaviour. From literature, hardness values in as-built IN718 samples tend to be susceptible to reheating effects: hardness decreases in the top part and increases at the bottom of SLM printed specimens. This is due to thermal effects: during deposition, solidified layers thermally affect the molten pool, triggering ageing of the material. As a result, the strengthening γ' and γ'' phases precipitate, reducing the Laves phases in the bottom part of samples and affecting the hardness values in different regions of the specimen.[26]

DOI: 10.13009/EUCASS2023-689

Table 5: Hardness measurements in HV: the three readings are averaged to obtain a mean value of results.

Sample	Reading 1	Reading 2	Reading 3	Mean Value, [HV]
1	342	333	314	330
2	320	294	301	305
3	327	326	321	325
4	322	327	303	317
5	324	328	326	326
7	327	333	338	333
8	319	334	336	330
10	332	336	328	330
11	330	337	331	333
12	335	329	327	330
13	346	339	325	337

3.1.3 Body Parameters Comparison and Selection

Following the overall analysis of densification, microstructure and hardness of the material, a selection can be performed considering the parameter windows detailed in Table 2. As within space applications full dense parts with consistent isotropy of body microstructure are needed, the most suitable parameters to be selected shall rely on the highest values of densification and hardness, with consistent microstructure. A comparison among the sample results leads to the following considerations:

1. Some of the samples have been discarded due to clear lower hydrostatic density values. It is the case of samples 6, 9, 14 and 15, which were neglected after plate distribution analysis. Contrarily to what assumed, as parameters dependence on the build disposition is negligible, no parameters were discarded due to asymmetries in densification values among the four build job areas.

2. Considering samples 2, 8, 5, 3 and 4, their density values among the eleven samples are significantly lower (below or equal to 99.5%). Thus, these samples can be neglected.

3. From micrographic images, samples 10 and 12 present significant flattened melting pools with respect to other specimens. These specimens can be discarded, as this phenomenon may affect the mechanical behaviour of the material.

4. From the comparison on the remaining samples, sample 7 is discarded due to reduced power values, which have been shown to impact densification of samples.

The trade-off considerations lead to the selection of sample 11, 1 and 13 as remaining body parameters. The choice among the three parameter groups shall rely on further tests, such as mechanical tensile tests and fatigue tests. The choice is mainly driven by the effects of power on the final density of the specimens, as it has been shown that higher laser power values tend to promote denser components. Samples with these parameters lead to less porosity and defects within metallographic sections. Finally, results in terms of hardness of the three specimens are consistent with full IN718 samples printed with SLM technology.

3.2 Contour Results

Contour specimens have been evaluated in their nominal dimension, inclination and final quality of the printed samples. The target of the analysis is the definition of proper hatch zone border and border parameters, as defined in Figure 1.

3.2.1 Dimensional Effects

After printing, preliminary visual inspection of the samples show absence of significant defects due to wrong processing window or due to recoater damages. Samples were subjected to **dimensional tests** on lateral length and inclination, as reported in Figure 1. Lateral length was evaluated by means of a micrometer, while the inclination of the sample wall was measured by means of a Coordinate Measuring Machine (CMM) Global S from Hexagon. Length and inclination measurements are summarized in Figure 12 and 13 respectively. Starting from lateral length results, it is evident that a correlation between the measurements and the assigned contour parameters holds. The dependency from the assigned contour parameters is confirmed from the graphs shown in Figure 12:

DOI: 10.13009/EUCASS2023-689

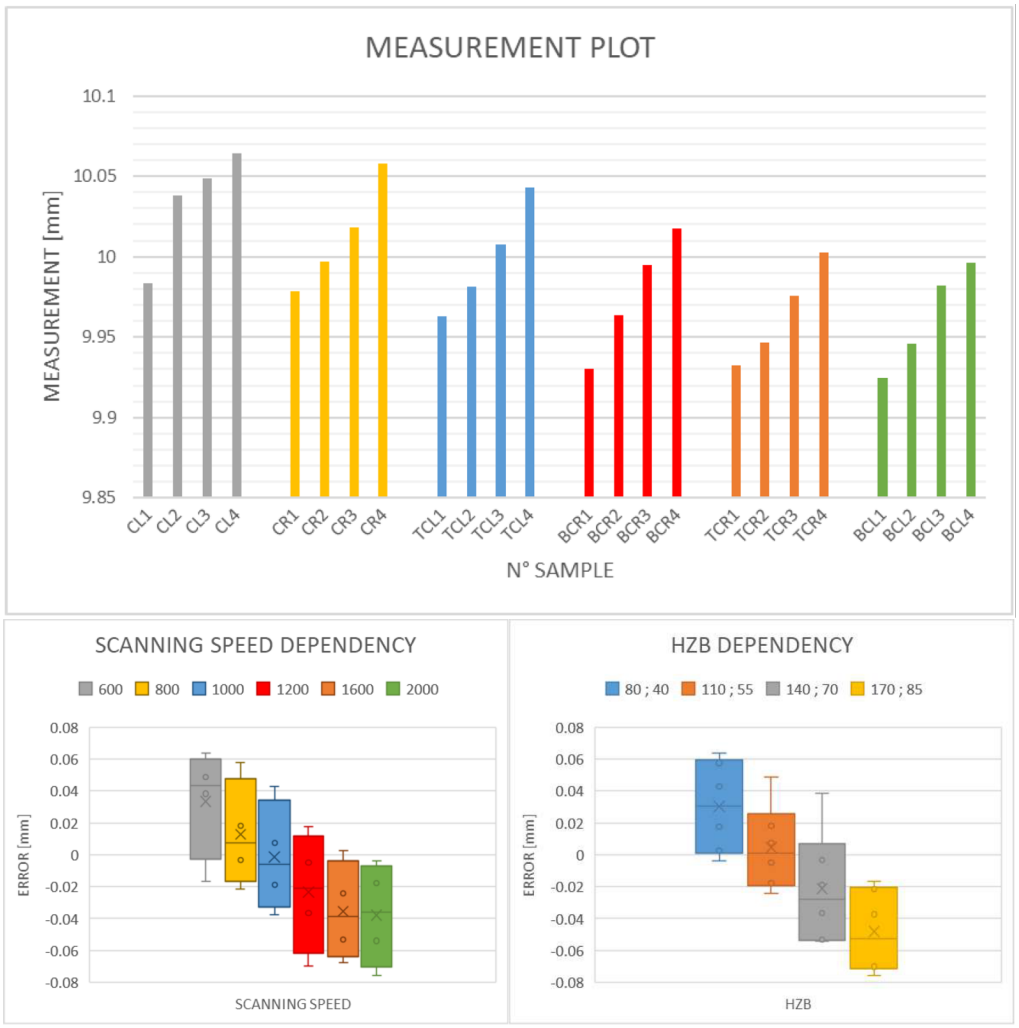

Figure 12: Inclined wall samples, nominal length measurements: on top, dimensions of the measured samples. Box plots: on the left, scanning speed dependency; on the right, HZB dependency.

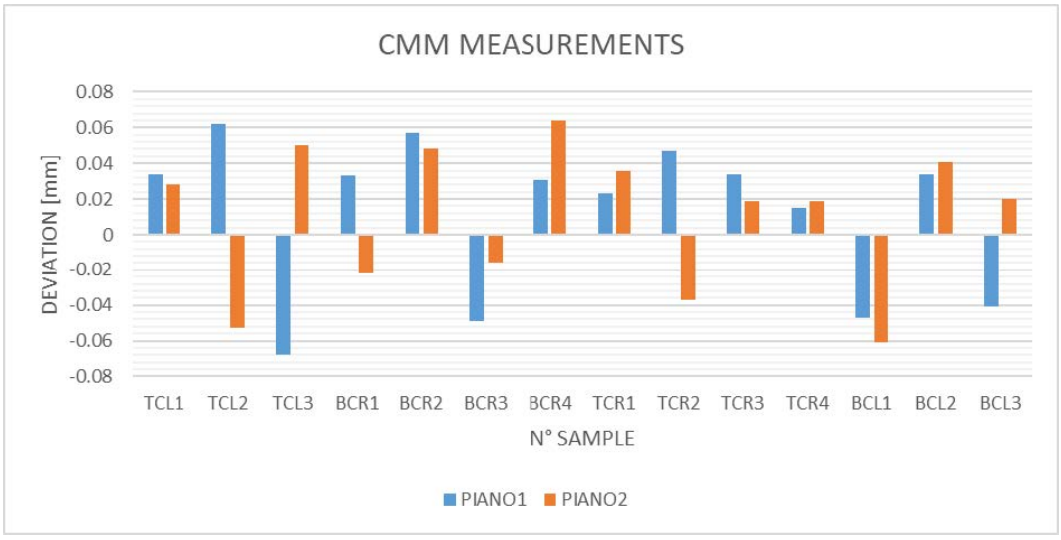

Figure 13: Inclined wall samples, nominal inclination measurements: CMM deviations. Samples with defects are discarded.

DOI: 10.13009/EUCASS2023-689

- The nominal dimension decreases with increasing scanning speed: there is a reduction of the linear energy density, which in turn results in fewer particles melted during the scanning process.

- The nominal dimension decreases with increasing offset parameters (HZB and border).

Results concerning the deviations from the nominal inclination (45 degrees) for each sample are summarized in Figure 13. They confirm that limited to no dependency between external sample inclination and the assigned contour parameters holds. Some of the samples reported superficial defects as it was not possible to recover the deviation values for the entire CL and CR families. The root cause may be related to recoater blade issues or to increased contour LED values coupled with the overhang angle of the surface under analysis: as powder is characterized by lower values of thermal conductivity, heat accumulation occurs at the surface edge of inclined walls.[27] When the thermal stress overcomes the material strength, then plastic deformation arises, which is measured as an increase in surface roughness or superficial defect. These effects may be confirmed by further superficial roughness measurements performed on each inclined surface.

3.2.2 Contour Parameters Comparison and Selection

From previous considerations on dimensional results, a preliminary selection of the range of contour parameters which satisfy the final dimensions needed for the samples can be made. The following considerations hold:

1. Concerning nominal length, at least one sample of each scan speed family targets the required dimension and minimizes the error. In particular, samples from CL and BCL families report almost all higher and lower dimensions, as detailed in Figure 12. This is due to their lower and higher scan speeds respectively: thus, they can be discarded in the analysis.

2. Concerning inclination, defects did not allow to obtain correct measurements when dealing with CL and CR families, as reported in Figure 13: this implies that lower scan speeds lead to surface issues. These families can be neglected in further analyses.

After previous considerations, samples BCR3 and TCR4 stand as main candidates for contour parameters. They report correct nominal length and show consistent inclination measurement. However, the trade-off choice among the two parameters shall consider more in-depth testing: in particular, surface roughness tests shall be performed in order to further quantify the external quality of each sample.

4. Conclusions

This work has presented a characterization analysis of as-printed IN718 samples through a SLM machine for space propulsive applications. Three jobs were printed containing different specimens for process parameters characterization: laser power, scan speed, hatch space were varied, while laser spotsize and layer thickness were fixed. Results in terms of densification, microstructure, defect distribution, hardness and final sample dimensions were retrieved and compared. Body and contour were analysed separately with cubes and inclined walls samples respectively.
Regarding cubic specimens, dimensional results were retrieved showing similar data among specimens: this is an expected result, as in skin-core strategies body parameters do not significantly affect external dimensions. Densification results are impacted by the selected parameters, in particular from laser power. No effects of plate disposition was registered, suggesting that major effects can be imputed to process paramaters rather than to the position on the plate. Furthermore, porosity percentages show improved values, even below <0.5% porosity for certain specimens. Micrographic images confirmed the correct window for hatch space, as all specimens reported consistent overlapping regions between melt pools. Critical defects, such as lack of fusion, open pores and gas entrainments were identified and imputed to the parameters as well. Vickers hardness values were consistent to literature results on printed IN718 samples for all specimens. Quantitative defect analysis supported by qualitative analyses were utilized to identify the body parameters capable of producing nearly defect-free IN718 components: in particular, parameters associated to specimens 11, 1 and 13 were retrieved.
From the analysis of contour samples, a clear dependency on sample inclination and contour parameters was not reported. Some of the sample show significant superficial defects, probably related to the selected parameters with the required overhang angle, which didn't allow the CMM measurements. On the other side, nominal dimension results demonstrated a relation between HZB and border parameters with the contour scan speed, as the nominal length tends to diminish with increased scan speed values. The analysis drove the selection towards sample parameters BCR3 and TCR4.

DOI: 10.13009/EUCASS2023-689

More testing is needed in order to complete the body and the contour parameters selection. First, an in-depth characterization of the generation of defects, including the evaluation of relations between body parameters and densification of samples, has to be performed. This shall be retrieved with dedicated Scanning Electron Microscope (SEM) images to investigate different phenomena: the melt pools border and the generation of defects in these areas; the characterisation of the overheating regions between melting pools; the evaluation of the melting pools boundaries and oxidation effects on microstructure.[7,15,22] Specific single track tests shall be performed to confirm the depth and width of different parameters on melting pools.[4,25] All the considerations on microstructure shall be corroborated by further mechanical tests on the specimens built using the same body parameters. On contour analyses, further considerations shall be made in order to confirm the selected parameters and the effects on surface roughness of inclined samples. Process parameters shall be tailored using surface roughness as design driver, as evidencied in other studies.[20] Furthermore, the analysis of the overlap region between contour and body shall be assessed through dedicated experiments in order to avoid the formation of sub-skin defects in the final material. Through these dedicated future tests, the definition of high-quality space propulsion parts would significantly benefit by means of tailored optimized machine parameters.

5. Acknowledgments

The authors want to aknowledge D-Orbit SpA company for the availability in the access to the machines involved in the SLM process of the samples; Sòphia High Tech srl company, for the support during manufacturing and postprocessing of the samples; TEC Eurolab srl company, for the support during specimen testing and analysis.

References

[1] Paul Gradl, Omar Mireles, and Nathan Andrews. Intro to additive manufacturing for propulsion systems. In *AIAA Joint Propulsion Conference*, number M18-6849, 2018.

[2] Paul Gradl. Metal additive manufacturing developments for propulsion applications. In *Team Redstone Additive Manufacturing (AM) Integrated Product Team (IPT)*, 2022.

[3] Byron Blakey-Milner, Paul Gradl, Glen Snedden, Michael Brooks, Jean Pitot, Elena Lopez, Martin Leary, Filippo Berto, and Anton du Plessis. Metal additive manufacturing in aerospace: A review. *Materials & Design*, 209:110008, 2021.

[4] Pankaj Kumar, Jano Farah, Javed Akram, Chong Teng, Jon Ginn, and Mano Misra. Influence of laser processing parameters on porosity in inconel 718 during additive manufacturing. *The International Journal of Advanced Manufacturing Technology*, 103:1497–1507, 2019.

[5] Salome Sanchez, Peter Smith, Zhengkai Xu, Gabriele Gaspard, Christopher J. Hyde, Wessel W. Wits, Ian A. Ashcroft, Hao Chen, and Adam T. Clare. Powder bed fusion of nickel-based superalloys: A review. *International Journal of Machine Tools and Manufacture*, 165:103729, 2021.

[6] Paul Gradl, Darren C Tinker, Alison Park, Omar R Mireles, Marissa Garcia, Ryan Wilkerson, and Christopher Mckinney. Robust metal additive manufacturing process selection and development for aerospace components. *Journal of Materials Engineering and Performance*, 31(8):6013–6044, 2022.

[7] Qingbo Jia and Dongdong Gu. Selective laser melting additive manufacturing of inconel 718 superalloy parts: Densification, microstructure and properties. *Journal of Alloys and Compounds*, 585:713–721, 2014.

[8] M Sundararaman, P Mukhopadhyay, and S Banerjee. Carbide precipitation in nickel base superalloys 718 and 625 and their effect on mechanical properties. *Superalloys*, 718:625–706, 1997.

[9] Ruidi Li, Jinhui Liu, Yusheng Shi, Li Wang, and Wei Jiang. Balling behavior of stainless steel and nickel powder during selective laser melting process. *The International Journal of Advanced Manufacturing Technology*, 59:1025–1035, 2012.

[10] Mohamed Balbaa, Sameh Mekhiel, Mohamed Elbestawi, and Jeff McIsaac. On selective laser melting of inconel 718: Densification, surface roughness, and residual stresses. *Materials & Design*, 193:108818, 2020.

[11] Luke Scime and Jack Beuth. Melt pool geometry and morphology variability for the inconel 718 alloy in a laser powder bed fusion additive manufacturing process. *Additive Manufacturing*, 29:100830, 2019.

DOI: 10.13009/EUCASS2023-689

[12] Nikolaos Kladovasilakis, Paschalis Charalampous, Konstantinos Tsongas, Ioannis Kostavelis, Dimitrios Tzovaras, and Dimitrios Tzetzis. Influence of selective laser melting additive manufacturing parameters in inconel 718 superalloy. *Materials*, 15(4):1362, 2022.

[13] Wenquan Wang, Suyu Wang, Xinge Zhang, Fei Chen, Yuxin Xu, and Yingtao Tian. Process parameter optimization for selective laser melting of inconel 718 superalloy and the effects of subsequent heat treatment on the microstructural evolution and mechanical properties. *Journal of Manufacturing Processes*, 64:530–543, 2021.

[14] J.H. Yi, J.W. Kang, T.J. Wang, X. Wang, Y.Y. Hu, T. Feng, Y.L. Feng, and P.Y. Wu. Effect of laser energy density on the microstructure, mechanical properties, and deformation of inconel 718 samples fabricated by selective laser melting. *Journal of Alloys and Compounds*, 786:481–488, 2019.

[15] Pravin Kumar, P Chakravarthy, Sushant K Manwatkar, and SVS Narayana Murty. Effect of scan speed and laser power on the nature of defects, microstructures and microhardness of 3d-printed inconel 718 alloy. *Journal of Materials Engineering and Performance*, 30(9):7057–7070, 2021.

[16] Linqing Liu, Di Wang, Yongqiang Yang, Zhi Wang, Zeyu Qian, Shibiao Wu, Jinrong Tang, Changjun Han, and Chaolin Tan. Effect of scanning strategies on the microstructure and mechanical properties of inconel 718 alloy fabricated by laser powder bed fusion. *Advanced Engineering Materials*, 25(5):2200492, 2023.

[17] Wang Di, Yang Yongqiang, Su Xubin, and Chen Yonghua. Study on energy input and its influences on single-track, multi-track, and multi-layer in slm. *The International Journal of Advanced Manufacturing Technology*, 58:1189–1199, 2012.

[18] Eyob Messele Sefene. State-of-the-art of selective laser melting process: A comprehensive review. *Journal of Manufacturing Systems*, 63:250–274, 2022.

[19] Rui Wang, Chaoyue Chen, Mingyu Liu, Ruixin Zhao, Songzhe Xu, Tao Hu, Sansan Shuai, Hanlin Liao, Linda Ke, Kim Vanmeensel, Jiang Wang, and Zhongming Ren. Effects of laser scanning speed and building direction on the microstructure and mechanical properties of selective laser melted inconel 718 superalloy. *Materials Today Communications*, 30:103095, 2022.

[20] Galina Kasperovich, Ralf Becker, Katia Artzt, Pere Barriobero-Vila, Guillermo Requena, and Jan Haubrich. The effect of build direction and geometric optimization in laser powder bed fusion of inconel 718 structures with internal channels. *Materials & Design*, 207:109858, 2021.

[21] Caroline A. Schneider, Wayne S. Rasband, and Kevin W. Eliceiri. Nih image to imagej: 25 years of image analysis. *Nature methods*, 9(7):671–675, 2012.

[22] Yin Xie, Qing Teng, Muyu Shen, Zhenyu Zhang, Yu Wei, Chao Cai, and Qingsong Wei. The role of overlap region width in multi-laser powder bed fusion of hastelloy x superalloy. *Virtual and Physical Prototyping*, 18(1), 2023.

[23] Mujian Xia, Dongdong Gu, Guanqun Yu, Donghua Dai, Hongyu Chen, and Qimin Shi. Porosity evolution and its thermodynamic mechanism of randomly packed powder-bed during selective laser melting of inconel 718 alloy. *International Journal of Machine Tools and Manufacture*, 116:96–106, 2017.

[24] Rashmi Priya Parida and V. Senthilkumar. Experimental studies of defect generation in selective laser melted inconel 718 alloy. *Materials Today: Proceedings*, 39:1372–1377, 2021. 2nd International Conference on Recent Trends in Metallurgy, Materials Science and Manufacturing.

[25] Jincheng Wang, Rui Zhu, Yujing Liu, and Laichang Zhang. Understanding melt pool characteristics in laser powder bed fusion: An overview of single- and multi-track melt pools for process optimization. *Advanced Powder Materials*, 2(4):100137, 2023.

[26] Wakshum M. Tucho, Priscille Cuvillier, Atle Sjolyst-Kverneland, and Vidar Hansen. Microstructure and hardness studies of inconel 718 manufactured by selective laser melting before and after solution heat treatment. *Materials Science and Engineering: A*, 689:220–232, 2017.

[27] Di Wang, Yongqiang Yang, Ziheng Yi, and Xubin Su. Research on the fabricating quality optimization of the overhanging surface in slm process. *The International Journal of Advanced Manufacturing Technology*, 65:1471–1484, 2013.